GDCh Research Article Angewandte International Edition Chemie www.angewandte.org

How to cite: *Angew. Chem. Int. Ed.* **2025**, *64*, e202504618
doi.org/10.1002/anie.202504618

Coordination Polymers

Liquid Coordination Polymers with Anhydrous Proton Conductivity

Nattapol Ma, Soracha Kosasang, Satoshi Horike, and Hiroki Yamada*

Abstract: Liquid states in coordination polymers (CPs) and metal-organic frameworks (MOFs) are typically considered transient intermediates in the crystal-to-glass transformations of organic–inorganic hybrid materials. However, their potential as functional materials has remained largely unexplored. Inspired by the unique properties of ionic liquids, organic liquids, and liquid metals, we explore liquid CPs as a platform for novel functionalities distinct from those of their crystalline and glass counterparts. Here, we present a strategy to achieve functional liquid CPs near ambient conditions by introducing H_3PO_4 as a network modifier, shifting compositions away from stoichiometric ratios. This process disrupts extended coordination networks during melting, producing a stable liquid state. By tuning the ratio of network modifiers, we achieve control over liquid properties, including anhydrous proton conductivity up to 27 mS cm^{-1} at 353 K and viscosities ranging from 18.8 to $10^{5.9}$ Pa·s at 303 K. These findings demonstrate the transformative potential of liquid CPs, introducing them as a new platform for designing liquid conductors.

Introduction

Solid-to-liquid transition is one of the most fundamental processes in material sciences, yet it is among the most complex phenomena to predict.[1] This process opens up opportunities not only for advanced material processing but also allows access to their unique properties.[2–4] For example, the discovery of liquid crystals has transformed display technologies by harnessing their anisotropic optical properties and stimuli responsiveness in fluid phases.[5] Similarly, ionic liquids have emerged as versatile solvents and electrolytes due to their low volatility, high thermal stability, and availability in a wide variation of physicochemical properties.[6]

[*] N. Ma
International Center for Young Scientists (ICYS), National Institute for Materials Science, 1-1 Namiki, Tsukuba, Ibaraki 305-0044, Japan
E-mail: ma.nattapol@nims.go.jp

S. Kosasang, S. Horike
Department of Chemistry, Graduate School of Science, Kyoto University, Kitashirakawa-oiwake-cho, Sakyo-ku, Kyoto 606–8502, Japan

S. Horike
Department of Materials Science and Engineering, School of Molecular Science and Engineering, Vidyasirimedhi Institute of Science and Technology, Rayong 21210, Thailand

H. Yamada
Diffraction and Scattering Division, Japan Synchrotron Radiation Research Institute (JASRI) Sayo, Hyogo 679–5198, Japan

Additional supporting information can be found online in the Supporting Information section

Proton and ionic conductivities in liquid systems are often described by Walden's rule, which outlines an inverse relationship between conductivity and viscosity.[7,8] While the concept provides a foundational understanding of ion transport in liquids, it also highlights a critical limitation: conductivity in liquid systems is predominantly governed by viscosity. In discrete molecular liquids, such as protic ionic liquids, the Walden plot generally classifies their conductivity as "ionic" or "subionic," where ion transport primarily occurs through the migration of low molecular-weight entities (vehicle mechanism).[6,9,10] However, this process is inherently less efficient than the structural diffusion (Grotthuss) mechanism observed in "superionic" conductors.[10] Efforts to enhance conductivity efficiency often involve reducing the migration of unwanted counterions via selective polymerization, observed in polymerized ionic liquids.[11,12] However, this comes at the expense of fluidity. These challenges emphasize the need for new liquid material platforms capable of overcoming the viscosity-conductivity trade-off.

Solid-to-liquid-to-glass transformation in some proton-conductive coordination polymers (CPs) and metal-organic frameworks (MOFs) presents an appealing solution for overcoming the limitation of liquid conductors.[13–17] Preservation of coordination networks even above the melting point helps restrict the migration of molecular entities, enabling selective proton migration and promoting the probability of achieving "superionic" behaviors.[18–20] Furthermore, compositional flexibility in these amorphous CPs/MOFs allows for continuous property control by incorporating diverse functional components. For instance, doping small amounts of stimuli-responsive molecules, such as pyranine or tris(bipyrazine)ruthenium(II), allows dynamic control over anhydrous proton conductivity in zinc–phosphate–azole CP glasses.[21,22] The physical properties, including melting and glass transition temperatures, can also be controlled by adjusting the composition of the resulting glass away from

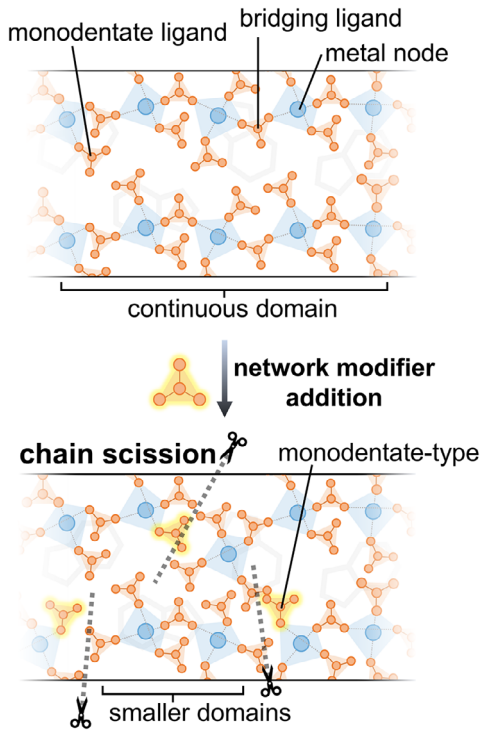

Figure 1. Schematic illustration of the proposed chain scission process in this work induced by the addition of network modifiers.

stoichiometric ratios.[23–30] Although functional liquids are common in many material families, they remain exotic within the context of CPs/MOFs.[31] Since the early observation of melting behavior in CPs/MOFs, liquid states have been viewed primarily as intermediates for accessing glassy states, mainly because the liquid states are exclusively observed at high temperatures.[32] For examples, zeolite imidazolate frameworks typically melt at 643–863 K,[24,33] while zinc–phosphate–azole CPs, despite having lower melting temperatures, still require at least ca. 370 K to become liquids.[14] To date, no functional liquid CPs have been reported near ambient conditions.[32,34]

This article presents a strategy for synthesizing liquid CPs by adjusting the equivalent amount of H_3PO_4 as a network modifier. Inspired by viscosity modulation in oxide glasses with network modifier additions,[35,36] we propose that substituting bridging phosphate ligands with terminal phosphate ligands in meltable zinc–phosphate–azole CPs similarly reduces the viscosity of CP glasses, allowing them to behave as network-forming liquids near ambient conditions (Figure 1). Here, the "liquid" state is defined based on viscosity-dependent flow properties, beginning at viscosities below the practical melting threshold ($\eta < 10$ Pa·s).[37,38] Properties such as anhydrous proton conductivity and viscosity are finely tuned by adjusting the network domain size and local structure through specific starting compositions. Despite variations in their macroscopic properties, pair distribution function analysis reveals that the short-to-intermediate range structures of all modified samples remain consistent with those of their parent CPs. This work highlights a versatile approach for designing liquid CPs with tunable functional properties.

Results and Discussion

Synthesis and Melting Behavior

A meltable CP, $[Zn_3(H_2PO_4)_6(H_2O)_3]$(1,2,3-benzotriazole) (Figure S1), was chosen as a representative material due to its low melting temperature among glass-forming CPs and MOFs.[18] This compound, referred to as ZnPBTA', was synthesized on a gram scale using a mechanochemical approach with a Teflon milling set, followed by dehydration to remove residual water (see Methods in SI). A series of non-stoichiometric CPs were prepared by reacting 3 mol equivalents of ZnO, 1 mol equivalent of 1,2,3-benzotriazole, and varying amounts of H_3PO_4. The H_3PO_4 used were 7.75, 9.5, and 11.25 mol equivalents for ZnPBTA'-m1, ZnPBTA'-m2, and ZnPBTA'-m3, respectively, compared to the stoichiometric ratio of 6 mol equivalents in ZnPBTA (Table S1). Powder X-ray diffraction (PXRD) patterns of the as-synthesized ZnPBTA'-m1, ZnPBTA'-m2, and ZnPBTA'-m3 matched well with the original ZnPBTA' (Figure S2). After dehydration, polycrystalline products were obtained (Figure S3). The dehydrated forms of ZnPBTA', ZnPBTA'-m1, ZnPBTA'-m2, and ZnPBTA'-m3 are denoted as ZnPBTA, ZnPBTA-m1, ZnPBTA-m2, and ZnPBTA-m3, respectively (Figure S4). PXRD analysis of the dehydrated samples suggests a structural change originating from the transformations around Zn^{2+} due to the release of water molecules from the octahedral coordination sphere.[18,39] However, the exact crystal structure of dehydrated ZnPBTA could not be determined, as the compound lost single crystallinity upon dehydration.[39] ^{31}P magic-angle spinning nuclear magnetic resonance (^{31}P MAS NMR, Figure S5) spectra of ZnPBTA-m1, ZnPBTA-m2, and ZnPBTA-m3 exhibit peaks exclusively within the orthophosphate range, indicating that no condensation occurs during the dehydration process and that all phosphate remains either anionic or in the form of free orthophosphoric acid.[40,41] Energy-dispersive spectroscopy (EDS) analysis further confirmed the absence of Teflon contamination in the dehydrated products (Figure S6). Additionally, the actual Zn/P mol fractions, analyzed by inductively coupled plasma optical emission spectroscopy (ICP-OES) technique, are provided in Table S2. FTIR spectra showed no distinct changes among the samples (Figure S7). These results suggest that ZnPBTA-m1, ZnPBTA-m2, and ZnPBTA-m3 comprise crystalline ZnPBTA domains alongside amorphous H_3PO_4.[22,27]

Heating crystalline ZnPBTA above its melting temperature ($T_{m,peak}$ = 394.6 K) produces a liquid state that remains stable up to 448 K (Figures S8 and S9). Differential scanning calorimetry (DSC, Figure S8) indicates that deviations from the stoichiometric composition result in changes in melting behavior, attributed to flux melting.[42,43] A similar melting temperature depression is observed in some multicomponent zeolitic imidazolate frameworks.[44,45] Upon heating, ZnPBTA-m1, ZnPBTA-m2, and ZnPBTA-m3

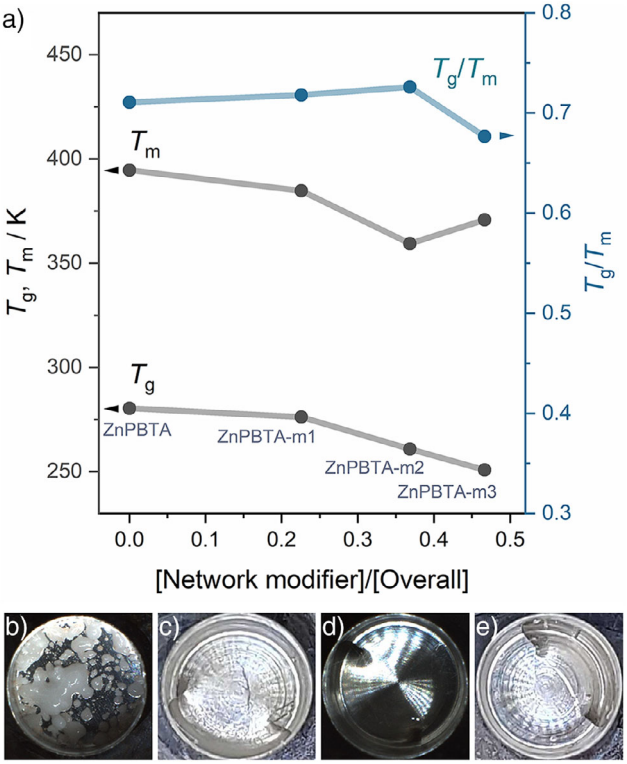

Figure 2. a) Melting temperature (T_m), glass transition temperature (T_g), and T_g/T_m as a function of the molar ratio of network modifier to overall H_3PO_4. T_m and T_g were determined from melting peak temperature and the temperature at which viscosity reached 10^{12} Pa·s, respectively. Optical images of b) ZnPBTA-g, c) ZnPBTA-g-m1, d) ZnPBTA-g-m2, and e) ZnPBTA-g-m3 at 393 K.

undergo simultaneous endothermic events corresponding to melting, dissolution, and depolymerization, with the overall enthalpy changes increasing proportionally to the excess H_3PO_4 content (Table S3). The melting process begins at onset temperatures of approximately 341–344 K, initiated by the partial dissolution of crystalline domains into the H_3PO_4 flux. This continues until endset temperatures of 390.5, 364.7, and 374.1 K for ZnPBTA-m1, ZnPBTA-m2, and ZnPBTA-m3, respectively. The peak melting temperature ($T_{m,\,peak}$), defined as the temperature at the peak of the DSC curve, decreases to 384.7 K for ZnPBTA-m1 and 359.4 K for ZnPBTA-m2 due to increased H_3PO_4 flux content, which facilitates solid-to-liquid transition via dissolution (Figure 2a). However, when the modifier content exceeds the saturation point, changes in flux composition lead to a slight increase in $T_{m,\,peak}$ to 370.7 K for ZnPBTA-m3.[46] Subsequent DSC heating reveals glass transition temperatures ($T_{g,\,DSC}$) of 282.4 and 280.7 K for ZnPBTA and ZnPBTA-m1, respectively. The T_g values for ZnPBTA-m2 and ZnPBTA-m3 fall below the measurement limit and are discussed in the next section. Thermogravimetric analysis (TGA) results show that all samples exhibit less than 1% weight loss up to at least 423 K, confirming the absence of phosphate condensation during the melt-quenching process (Figures S9–S13). Additionally, changes in the character of the liquid states were observed at 393 K, where they became transparent with increasing amounts of H_3PO_4 beyond the stoichiometric limit (Figure 2b–e). Upon quenching to room temperature, ZnPBTA-g and ZnPBTA-g-m1 solidified into an amorphous solid, while ZnPBTA-g-m2 and ZnPBTA-g-m3 remained as viscous liquids. Note that -g indicates samples after melting. The PXRD patterns of all melt-quenched samples exhibited no Bragg peaks, confirming the absence of long-range orders, and are homogeneous without any detectable crystalline H_3PO_4 (Figure S14).

Viscosity and Glass Transition

The liquid-like behavior at lower temperatures with excess H_3PO_4 motivated us to quantify changes in viscosity. The viscosity of all samples follows a MYEGA-like temperature dependence, with glass transition temperatures (T_g) estimated by extrapolating viscosity to 10^{12} Pa·s (Figure 3a, Table S4).[47,48] A clear decreasing trend in T_g was observed with increasing H_3PO_4 content, resulting in T_g values of 280.4, 276.2, 260.9, and 250.8 K for ZnPBTA-g, ZnPBTA-g-m1, ZnPBTA-g-m2, and ZnPBTA-g-m3, respectively. These results align with the $T_{g,dsc}$ values obtained from DSC measurements for ZnPBTA-g and ZnPBTA-g-m1.

At higher temperatures, the viscosity values drop below the working point ($\eta = 10^3$ Pa·s) at 312, 299, and 283 K for ZnPBTA-g-m1, ZnPBTA-g-m2, and ZnPBTA-g-m3, respectively. At this point, the viscosity is comparable to molten soda-lime glass at above 1373 K.[49] Additionally, practical melting temperatures ($\eta < 10$ Pa·s) are achievable at 360, 329, and 308 K for ZnPBTA-g-m1, ZnPBTA-g-m2, and ZnPBTA-g-m3. Below these temperatures, viscosity approaches the range typical of ionic liquids at their operating temperatures.[50] The reduced viscosity values further support the role of H_3PO_4 as a network modifier, inducing chain scission in the 1D coordination chains.[20] A similar decreasing trend of viscosity was observed in $Zn(HPO_4)(H_2PO_4)_2](H_2Im)_2$ upon introducing $CsHSO_4$, where oxyanion exchanging between HSO_4^- and bridging phosphate decreases overall viscosity.[27] Analogous behavior is also observed in conventional inorganic glasses, where increasing network modifier content continuously decreases viscosity.[51,52]

The liquid characteristics were further evaluated through a fragility diagram (Figure 3b), comparing the melt-quenched samples with references from various material families.[10,51,53–56] The fragility indexes (m) of the melt-quenched samples ranged from 118 to 146, positioning them between $ZnCl_2$, which exhibits intermediate fragility, and fragile H_3PO_4.[48] The high fragility is attributed to the relatively low viscosity near T_m, estimated at 0.5–5.5 Pa·s for the modified samples and $10^{2.7}$ Pa·s for ZnPBTA. In contrast, the strong ZIF-62 glass exhibits a much lower fragility index ($m = 23$) and an exceptionally high viscosity of $10^{5.5}$ Pa·s at T_m.[55] Another key parameter to describe the liquid behavior is the T_g/T_m ratio, which indicates the tendency of a liquid to form glass upon cooling rather than crystallizing.[38,57] ZnPBTA exhibits a T_g/T_m of 0.71. With increasing H_3PO_4 fractions, T_g/T_m initially increases, reaching

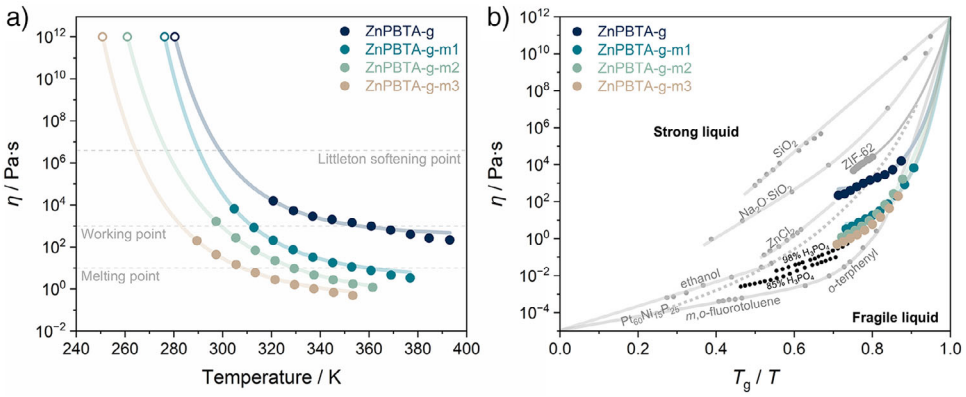

Figure 3. Viscosity of melt-quenched samples. a) Temperature-dependent viscosity of ZnPBTA-g, ZnPBTA-g-m1, ZnPBTA-g-m2, and ZnPBTA-g-m3 with MYEGA (Mauro-Yue-Ellison-Gupta-Allan)[47] fit. Fitting parameters are listed in Table S4. b) Fragility plot of melt-quenched samples in comparison with reference compounds. Data of reference compounds are taken from ref. [10, 51, 53–56]

a maximum of 0.73 for ZnPBTA-m2, before decreasing to 0.67 for ZnPBTA-m3 due to its higher T_m.

Short-to-intermediate Range Order

Having observed alterations in viscosity and thermal behaviors, we further focused on examining the role of the network modifier (H_3PO_4) in inducing changes to the local structure of the modified samples compared to the pristine ZnPBTA. We probed the short-to-intermediate range order in all samples before and after melt-quenching using pair-distribution function (PDF) analyses, which provide the probability of finding atomic pair distances presented as weighted histograms (Figure 4).[58] Despite slight intensity differences below 5 Å, the peak features of the crystalline derivatives remained largely identical to the pristine ZnPBTA, highlighting the retention of short-range order within crystalline domains (Figure 4c). Pair correlations from Zn^{2+} to its first and second nearest-neighbor Zn^{2+} appeared at ca. 3.3 Å ($Zn\cdots Zn^{1st}$) and 5.2–5.5 Å ($Zn\cdots Zn^{2nd}$), respectively (Table S5). These measured distances align well with the predicted values of 3.19 and 5.37 Å from the crystal structure of ZnPBTA' at 100 K.[18] The peak splitting observed in the $Zn\cdots Zn^{2nd}$ region of ZnPBTA, compared to the simulated PDF pattern of ZnPBTA' (Figure S16), was attributed to the deformation of the Zn^{2+} octahedral coordination sphere upon dehydration. With increasing H_3PO_4 content from ZnPBTA to ZnPBTA-m3, a gradual increase in peak intensity corresponding to the intramolecular P–O correlation at 1.5 Å was observed. A peak at ca. 3.9 Å and a recombined peak corresponding to the $Zn\cdots Zn^{2nd}$ correlation at 5.2–5.3 Å emerged with excess H_3PO_4, plausibly due to Zn^{2+} coordination with phosphate, which completes the octahedral coordination. A similar transformation occurred at ca. 7.5 Å ($Zn\cdots Zn^{3nd}$) when comparing ZnPBTA to ZnPBTA-m1. However, in ZnPBTA-m2 and ZnPBTA-m3, this $Zn\cdots Zn^{3nd}$ correlation was hindered, plausibly due to strong contributions from Zn···P, Zn···O, P···O, and O···O correlations from excess H_3PO_4 or increased structural disorder. A slight reduction in amplitude at ca. 2.1, 3.3, and 4.4 Å, corresponding to Zn–O, Zn···Zn/P, and O···Zn/P correlations, respectively, indicates a higher degree of disorder within the 1D chains. These peak assignments are supported by calculated partial PDFs derived from the crystal structure of ZnPBTA' (Figure 4e).[18,59]

After melt-quenching, the distinct peak features below 5 Å are preserved, although some positions and intensities shift compared to those of the parent crystals (Figures 4d, S17–S24). The shift in Zn–O correlations from 2.1 Å to below 2.0 Å suggests a transformation in the coordination environment of Zn^{2+}, from octahedral to tetrahedral geometry. This transformation is further supported by the diminished contributions from $Zn\cdots Zn^{1st}$ and $Zn\cdots Zn^{2nd}$, along with a shift in the Zn–P contribution from ca. 3.3 Å in the crystalline state to ca. 3.2 Å after melt-quenching. Additionally, a new peak emerges at ca. 5.8–5.9 Å (Table S6), representing a $Zn\cdots Zn^{1st}$ correlation unique to Zn-phosphate-azole CPs with tetrahedral geometry (Figure 4a–d).[14] To verify these peak assignments, we performed experimental and calculated partial PDF analyses of $[Zn(HPO_4)(H_2PO_4)_2](ImH_2)_2$ (H_2Im = imidazolium) in both crystalline (ZnPIm) and glassy (ZnPIm-g) states, which also feature tetrahedral coordination around Zn^{2+} (Figures S26 and S27).[13,14] Note that the calculated $Zn\cdots Zn^{1st}$ distance from the crystal structure of ZnPIm at 243 K is ca. 5.7 Å.[13]

Despite a significant change in viscosity, the short-to-intermediate-range features of the modified samples remain largely consistent with those of unmodified ZnPBTA-g (Figure 4d). The correlation at ca. 5.8 Å, corresponding to the $Zn\cdots Zn^{1st}$ pair, suggests that some degree of metal-ligand-metal connectivity is retained in all samples, even in ZnPBTA-g-m3 with the highest modifier content. However, the peak is relatively weak, indicating that the 1D coordination chains may undergo substantial scission, potentially fragmenting into much smaller species, including trimers, dimers, or even monomers, depending on the amount of Zn^{2+} in the coordination network.[20,60] Furthermore, the observed decrease in viscosity with increasing H_3PO_4 content supports extensive chain fragmentation, likely driven by

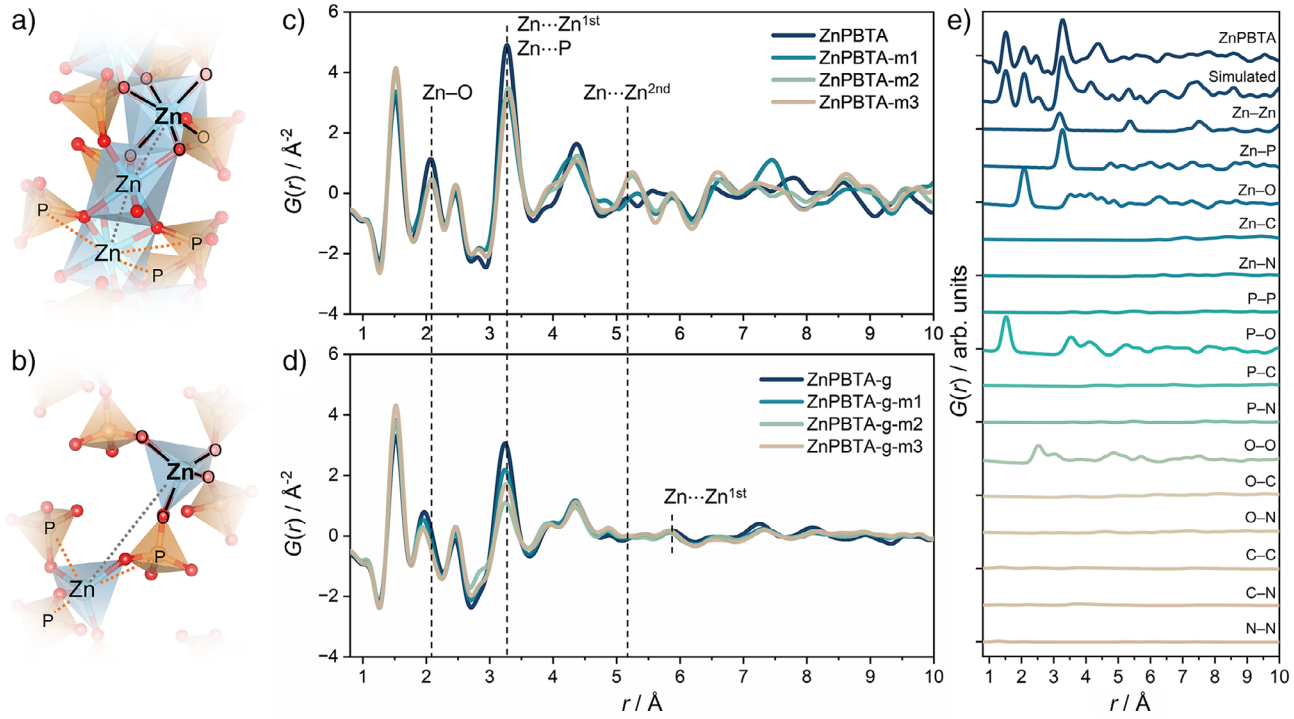

Figure 4. Local structure of modified samples. Local arrangements around Zn^{2+} in a) octahedral coordination[18] and b) tetrahedral coordination.[13] Zn, P, and O atoms are represented by light blue, orange, and red, respectively. Pair distribution function (PDF) of c) ZnPBTA, ZnPBTA-m1, ZnPBTA-m2, and ZnPBTA-m3 and d) ZnPBTA-g, ZnPBTA-g-m1, ZnPBTA-g-m2, and ZnPBTA-g-m3. $Zn\cdots Zn^{1st}$ and $Zn\cdots Zn^{2nd}$ represent pair correlation from Zn^{2+} to the first and second nearest neighbor Zn^{2+}, respectively. e) Simulated PDF and partial PDF of ZnPBTA. Additional S(Q) data and extended PDF data up to 30 Å are provided in Figures S16–S25 of the Supporting Information. Note that ZnPBTA-g shows partial recrystallization due to its fast crystallization under ambient conditions.[14]

anion exchange between bridging and terminal phosphate ligands.[27] At higher *r* distances, the melt-quenched samples exhibit peak broadening, reflecting a loss of periodicity.

Anhydrous Proton Conductivity

We measured the proton conductivity of melt-quenched samples using alternative current (AC) impedance spectroscopy under a dry Ar atmosphere. Samples in their molten state were loaded into a conductivity cell with fixed dimensions. For each measurement, the samples were heated to specific temperatures for at least 3 h and allowed to equilibrate until the conductivity values stabilized.

ZnPBTA exhibits Arrhenius-type behavior, with proton conductivity values of 3.3×10^{-4} mS cm^{-1} at 303 K and 5.7×10^{-3} mS cm^{-1} at 323 K.[18] An abrupt increase in proton conductivity was observed above 50 °C, reaching 9.0×10^{-2} mS cm^{-1} at 333 K and 1.2 mS cm^{-1} at 373 K. Below 60 °C, conductivity is primarily governed by the mobility of phosphate moieties along the 1D zinc-phosphate chains. Above this temperature, the random rotation of BTA molecules provides an additional contribution to proton conductivity, alongside enhanced phosphate dynamics, leading to a change in activation energy.[18] A similar abrupt change in proton conductivity upon heating has also been observed in other zinc-phosphate-azole CPs, such as $[Zn_3(H_2PO_4)_6(H_2O)_3]$(benzimidazole)[39] and $Zn(HPO_4)(H_2PO_4)_2](H_2Im)_2$.[13] After melt-quenching, ZnPBTA-g exhibits significantly enhanced conductivity, with values of 0.33 mS cm^{-1} at 303 K and 8.0 mS cm^{-1} at 393 K.[18]

By tuning the ratio of network modifiers, we achieved control over anhydrous proton conductivity (Figures 5a, S28–S34, and Table S7). The maximum proton conductivities of 13.8 mS cm^{-1} at 393 K, 17.2 mS cm^{-1} at 373 K, and 27 mS cm^{-1} at 353 K were achieved for ZnPBTA-g-m1, ZnPBTA-g-m2, and ZnPBTA-g-m3, respectively, all exceeding the 8.0 mS cm^{-1} measured for ZnPBTA-g at 393 K. Note that proton conductivity measurements for ZnPBTA-g-m2 and ZnPBTA-g-m3 could not be conducted above 373 and 353 K, respectively, as the samples began leaking in our setup due to their low viscosity. The temperature-dependent proton conductivity of the sample with stoichiometric composition transitions from Arrhenius-type behavior in crystalline ZnPBTA to Vogel–Fulcher–Tammann (VFT)-type behavior after melt-quenching.[61–63] The Arrhenius behavior, linked to activated local ion hopping in crystalline conductors, contrasts with the VFT behavior, which reflects ion migration coupled with structural dynamics and assisted by structural relaxation in amorphous glasses or polymers.[48] The obtained fitting parameters are summarized in Table S8. The VFT behavior is retained in ZnPBTA-g-m1 and ZnPBTA-g-m2, accompanied by an increase in proton conductivity. In these cases, additional network modifiers enhance structural dynamics, as

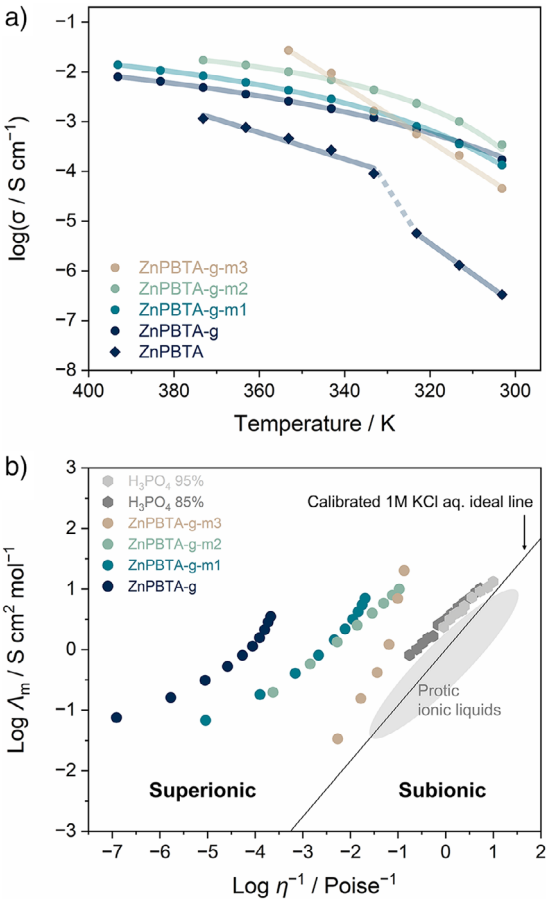

Figure 5. Anhydrous proton conductivity of melt-quenched ZnPBTA-g, ZnPBTA-g-m1, ZnPBTA-g-m2, and ZnPBTA-g-m3. a) Variable temperature proton conductivity under dry Ar atmosphere in comparison with crystalline ZnPBTA. Data of ZnPBTA and ZnPBTA-g are taken from ref. [18] Nyquist plots are available in Figures S28–S32 in the supporting information. b) Walden plots in comparison with 85%, 95% H_3PO_4, and protic ionic liquids. Reference data of H_3PO_4, protic ionic liquids, and calibrated ideal KCl line are taken from ref. [8, 10]

reflected in the decreased T_g values. We observed a decreasing trend in activation factors (B) and a smaller difference between the VFT-fitted ideal transition temperature (T_0) and T_g with increasing network modifier content. The former suggests weaker temperature dependence and lower barriers for proton conduction, while the latter indicates a reduced decoupling effect.[48,64–66] Further increases in network modifiers in ZnPBTA-g-m3 result in a transition back to Arrhenius-type behavior with a relatively high activation energy of 1.20 eV. This shift is likely driven by the dominant contributions of free H_3PO_4 and highly fragmented CP chains, as evidenced by a decrease in the measured density (Table S9). The observed activation energy aligns closely with those of crystalline ZnPBTA (1.22 eV) and $[Zn_3(H_2PO_4)_6](1,3$-benzimidazole) (1.5 eV), measured at temperatures below the threshold where azole molecules begin to rotate and contribute to proton conduction.[18,39]

The Walden plot was utilized to examine the relationship between viscosity (η), equivalent conductivity (Λ_m), and the proton-conductivity mechanisms.[6,67] In this study (Figure 5b), all samples deviate from Walden's ideal line, occupying the superionic region. Equivalent conductivities exceeding those predicted by Walden's rule indicate a decoupling of charge carriers from the overall structural networks that govern viscosity. This suggests that proton migration predominantly occurs via the Grotthuss mechanism. The weak dependence of conductivity on viscosity allows for the adjustment of viscosity without compromising high proton conductivity. As the content of the network modifier increases, the trend shifts closer to the ideal line of ionic conduction in a fluid-diluted solution.[8] Along this line, molar conductivity is directly proportional to the fluidity of the medium, indicating that ion migration is fully coupled with the structural dynamics.[48] The shift is attributed to reduced viscosity and an increased contribution from the vehicle mechanism, facilitated by free phosphoric acid and the formation of smaller coordination network fragments with higher H_3PO_4 content. These observations are consistent with the reduced decoupling effect identified in the VFT fitting analysis as the network modifier content increases. However, even with the highest modifier content (ZnPBTA-m3), the sample remains above phosphoric acid on the Walden plot (Figure 5b). This suggests that ZnPBTA-m3 still relies heavily on the Grotthuss mechanism for proton conductivity, similar to phosphoric acid (~97% Grotthuss contribution).[48,68,69]

Conclusion

This study presents a strategy for preparing liquid CPs near ambient conditions by shifting their composition away from stoichiometric ratios. Excess phosphate ligands act as network modifiers, enabling control over thermal behavior, proton conductivity, and viscosity. By varying the amount of network modifiers, we achieved tunable CP properties, including anhydrous proton conductivity ranging from 2.6 to 27 mS cm^{-1} at 353 K and viscosities from 18.8 to $10^{5.9}$ Pa·s at 303 K. Synchrotron X-ray total scattering and PDF analysis revealed a structural transformation in the coordination environment around Zn^{2+}, shifting from octahedral to tetrahedral geometry upon melt-quenching, with evidence of substantial chain fragmentation. This work thus establishes a foundation for designing next-generation functional liquid materials with tailored properties, offering an exciting platform for applications that demand flexibility, dynamic mixing capabilities, and intrinsic proton conductivity.

Supporting Information

The authors have cited additional references within the Supporting Information.[13,14,18,20,22,27,59,70–91]

Acknowledgements

N.M. acknowledges the support from ICYS for a research fellowship, from the Japan Society of the Promotion of Science (JSPS) for a Grant-in-Aid for Research Activity

Start-up (JP24K23109) and Grant-in-Aid for Early-Career Scientists (JP25K18055), and from the Sumitomo Foundation basic science grant number 2402150. The authors acknowledge BL04B2 beamlines at SPring-8 for the synchrotron X-ray total scattering experiments with the approval of JASRI (Proposal No. 2024B1167). They thank Dr. Takashi Nakanishi (NIMS) and Dr. Renzhi Ma (NIMS) for access to equipment. They thank Dr. Daiki Umeyama for discussions. They thank Nao Horike for ^{31}P MAS NMR measurements. They thank Yu Fujii for the ICP-OES analysis. They acknowledge support from the NIMS Surface and Bulk Analysis Unit and NIMS Nanofabrication Facilities.

Conflict of Interests

The authors declare no conflict of interest.

Data Availability Statement

The data that support the findings of this study are available from the corresponding author upon reasonable request.

Keywords: Amorphous materials · Coordination polymers · Liquids · Network modifiers · Proton conductivities

[1] K. Mochizuki, M. Matsumoto, I. Ohmine, *Nature* **2013**, *498*, 350–354.
[2] S. Santhosh Babu, J. Aimi, H. Ozawa, N. Shirahata, A. Saeki, S. Seki, A. Ajayaghosh, H. Möhwald, T. Nakanishi, *Angew. Chem. Int. Ed.* **2012**, *51*, 3391–3395.
[3] G. Cao, J. Liang, Z. Guo, K. Yang, G. Wang, H. Wang, X. Wan, Z. Li, Y. Bai, Y. Zhang, J. Liu, Y. Feng, Z. Zheng, C. Lu, G. He, Z. Xiong, Z. Liu, S. Chen, Y. Guo, M. Zeng, J. Lin, L. Fu, *Nature* **2023**, *619*, 73–77.
[4] Y. Wu, M. Li, Z.-g. Zheng, Z.-Q. Yu, W.-H. Zhu, *J. Am. Chem. Soc.* **2023**, *145*, 12951–12966.
[5] H. K. Bisoyi, Q. Li, *Chem. Rev.* **2022**, *122*, 4887–4926.
[6] C. Austen Angell, Y. Ansari, Z. Zhao, *Faraday Discuss.* **2012**, *154*, 9–27.
[7] P. Walden, *Z. Phys. Chem.* **1906**, *55U*, 207–249.
[8] C. Schreiner, S. Zugmann, R. Hartl, H. J. Gores, *J. Chem. Eng. Data* **2010**, *55*, 1784–1788.
[9] W. Xu, E. I. Cooper, C. A. Angell, *J. Phys. Chem. B* **2003**, *107*, 6170–6178.
[10] J.-P. Belieres, C. A. Angell, *J. Phys. Chem. B* **2007**, *111*, 4926–4937.
[11] R. Sun, M. Agrawal, K. C. Neyerlin, J. D. Snyder, Y. A. Elabd, *Macromolecules* **2022**, *55*, 6716–6729.
[12] C. M. Evans, G. E. Sanoja, B. C. Popere, R. A. Segalman, *Macromolecules* **2016**, *49*, 395–404.
[13] S. Horike, D. Umeyama, M. Inukai, T. Itakura, S. Kitagawa, *J. Am. Chem. Soc.* **2012**, *134*, 7612–7615.
[14] D. Umeyama, S. Horike, M. Inukai, T. Itakura, S. Kitagawa, *J. Am. Chem. Soc.* **2015**, *137*, 864–870.
[15] T. D. Bennett, J.-C. Tan, Y. Yue, E. Baxter, C. Ducati, N. J. Terrill, H. H. M. Yeung, Z. Zhou, W. Chen, S. Henke, A. K. Cheetham, G. N. Greaves, *Nat. Commun.* **2015**, *6*, 8079.
[16] Y.-J. Su, Y.-L. Cui, Y. Wang, R.-B. Lin, W.-X. Zhang, J.-P. Zhang, X.-M. Chen, *Cryst. Growth Des.* **2015**, *15*, 1735–1739.
[17] Y. Hirai, T. Nakanishi, Y. Kitagawa, K. Fushimi, T. Seki, H. Ito, H. Fueno, K. Tanaka, T. Satoh, Y. Hasegawa, *Inorg. Chem.* **2015**, *54*, 4364–4370.
[18] N. Ma, S. Kosasang, A. Yoshida, S. Horike, *Chem. Sci.* **2021**, *12*, 5818–5824.
[19] T. Ogawa, K. Takahashi, S. S. Nagarkar, K. Ohara, Y.-l. Hong, Y. Nishiyama, S. Horike, *Chem. Sci.* **2020**, *11*, 5175–5181.
[20] T. Ogawa, K. Takahashi, T. Kurihara, S. S. Nagarkar, K. Ohara, Y. Nishiyama, S. Horike, *Chem. Mater.* **2022**, *34*, 5832–5841.
[21] S. S. Nagarkar, S. Horike, T. Itakura, B. L.e Ouay, A. Demessence, M. Tsujimoto, S. Kitagawa, *Angew. Chem. Int. Ed.* **2017**, *56*, 4976–4981.
[22] N. Ma, S. Impeng, S. Bureekaew, N. Morozumi, M.-a. Haga, S. Horike, *J. Am. Chem. Soc.* **2023**, *145*, 9808–9814.
[23] L. Longley, S. M. Collins, C. Zhou, G. J. Smales, S. E. Norman, N. J. Brownbill, C. W. Ashling, P. A. Chater, R. Tovey, C.-B. Schönlieb, T. F. Headen, N. J. Terrill, Y. Yue, A. J. Smith, F. Blanc, D. A. Keen, P. A. Midgley, T. D. Bennett, *Nat. Commun.* **2018**, *9*, 2135.
[24] L. Frentzel-Beyme, M. Kloß, P. Kolodzeiski, R. Pallach, S. Henke, *J. Am. Chem. Soc.* **2019**, *141*, 12362–12371.
[25] V. Nozari, C. Calahoo, J. M. Tuffnell, D. A. Keen, T. D. Bennett, L. Wondraczek, *Nat. Commun.* **2021**, *12*, 5703.
[26] C. Thanaphatkosol, N. Ma, K. Kageyama, T. Watcharatpong, T. Tiyawarakul, K. Kongpatpanich, S. Horike, *Chem. Commun.* **2022**, *58*, 6064–6067.
[27] N. Ma, N. Horike, L. Lombardo, S. Kosasang, K. Kageyama, C. Thanaphatkosol, K. Kongpatpanich, K.-i. Otake, S. Horike, *J. Am. Chem. Soc.* **2022**, *144*, 18619–18628.
[28] S. S. Sørensen, X. Ren, T. Du, A. Traverson, S. Xi, L. R. Jensen, M. Bauchy, S. Horike, J. Wang, M. M. Smedskjaer, *Small* **2023**, *19*, 2205988.
[29] W.-L. Xue, P. Kolodzeiski, H. Aucharova, S. Vasa, A. Koutsianos, R. Pallach, J. Song, L. Frentzel-Beyme, R. Linser, S. Henke, *Nat. Commun.* **2024**, *15*, 4420.
[30] F. Cao, S. S. Sørensen, A. K. Christensen, S. Mollick, X. Ge, D. Sun, A. B. Nielsen, N. C. Nielsen, N. Lock, R. Lu, R. Klemmt, P. K. Kristensen, L. R. Jensen, F. Dallari, J. Baglioni, G. Monaco, M. A. Karlsen, V. Baran, M. M. Smedskjaer, *ChemRxiv* **2024**, ChemRxiv preprint https://doi.org/10.26434/chemrxiv-2024-bgf8b-v2.
[31] N. Ma, S. Horike, *Chem. Rev.* **2022**, *122*, 4163–4203.
[32] N. Ma, S. Kosasang, E. K. Berdichevsky, T. Nishiguchi, S. Horike, *Chem. Sci.* **2024**, *15*, 7474–7501.
[33] T. D. Bennett, Y. Yue, P. Li, A. Qiao, H. Tao, N. G. Greaves, T. Richards, G. I. Lampronti, S. A. T. Redfern, F. Blanc, O. K. Farha, J. T. Hupp, A. K. Cheetham, D. A. Keen, *J. Am. Chem. Soc.* **2016**, *138*, 3484–3492.
[34] R. Gaillac, P. Pullumbi, K. A. Beyer, K. W. Chapman, D. A. Keen, T. D. Bennett, F.-X. Coudert, *Nat. Mater.* **2017**, *16*, 1149–1154.
[35] C. Huang, A. N. Cormack, *J. Mater. Chem.* **1992**, *2*, 281.
[36] A. Bunde, K. Funke, M. D. Ingram, *Solid State Ion.* **1998**, *105*, 1–13.
[37] P. G. Debenedetti, F. H. Stillinger, *Nature* **2001**, *410*, 259–267.
[38] G. N. Greaves, S. Sen, *Adv. Phys.* **2007**, *56*, 1–166.
[39] D. Umeyama, S. Horike, M. Inukai, S. Kitagawa, *J. Am. Chem. Soc.* **2013**, *135*, 11345–11350.
[40] R. J. Kirkpatrick, R. K. Brow, *Solid State Nucl. Magn. Reson.* **1995**, *5*, 9–21.
[41] A. Viani, G. Mali, P. Mácová, *Ceram. Int.* **2017**, *43*, 6571–6579.
[42] G. Lusvardi, G. Malavasi, L. Menabue, M. C. Menziani, *J. Phys. Chem. B* **2002**, *106*, 9753–9760.
[43] S. Wang, E. Rani, F. Gyakwaa, H. Singh, G. King, Q. Shu, W. Cao, M. Huttula, T. Fabritius, *Inorg. Chem.* **2022**, *61*, 7017–7025.

[44] L. Longley, S. M. Collins, S. Li, G. J. Smales, I. Erucar, A. Qiao, J. Hou, C. M. Doherty, A. W. Thornton, A. J. Hill, X. Yu, N. J. Terrill, A. J. Smith, S. M. Cohen, P. A. Midgley, D. A. Keen, S. G. Telfer, T. D. Bennett, *Chem. Sci.* **2019**, *10*, 3592–3601.
[45] P. Kolodzeiski, B. M. Gallant, L. Richter, M. A. T. Ongkiko, C. Franke, A. Kostka, W.-L. Xue, C. Das, J.-B. Weiß, E. Kolodzeiski, T. Kress, G. Kieslich, T. Li, A. J. Morris, D. Kubicki, S. Henke, **2025**, ChemRxiv preprint https://doi.org/10.26434/chemrxiv-2025-3m7vv.
[46] H. Wang, T. Zhang, H. Zhu, G. Li, Y. Yan, J. Wang, *ISIJ Int.* **2011**, *51*, 702–706.
[47] J. C. Mauro, Y. Yue, A. J. Ellison, P. K. Gupta, D. C. Allan, *Proc. Natl. Acad. Sci. USA* **2009**, *106*, 19780–19784.
[48] Y. Wang, N. A. Lane, C.-N. Sun, F. Fan, T. A. Zawodzinski, A. P. Sokolov, *J. Phys. Chem. B* **2013**, *117*, 8003–8009.
[49] J. E. Shelby, *Introduction to Glass Science and Technology*, 2nd ed., Royal Society of Chemistry, Cambridge, UK, **2005**.
[50] G. Yu, D. Zhao, L. Wen, S. Yang, X. Chen, *AIChE J.* **2012**, *58*, 2885–2899.
[51] C. A. Angell, *Science* **1995**, *267*, 1924–1935.
[52] C. A. Angell, *MRS Bull.* **2008**, *33*, 544–555.
[53] C. A. Angell, C. T. Moynihan, M. Hemmati, *J. Non-Cryst. Solids* **2000**, *274*, 319–331.
[54] A. Takeuchi, H. Kato, A. Inoue, *Intermetallics* **2010**, *18*, 406–411.
[55] A. Qiao, T. D. Bennett, H. Tao, A. Krajnc, G. Mali, C. M. Doherty, A. W. Thornton, J. C. Mauro, G. N. Greaves, Y. Yue, *Sci. Adv.* **2018**, *4*, eaao6827.
[56] R. Conradt, in *Springer Handbook of Glass* (Eds.: J. D. Musgraves, J. Hu, L. Calvez), Springer International Publishing **2019**, Cham, pp. 51–77.
[57] K. Ito, C. T. Moynihan, C. A. Angell, *Nature* **1999**, *398*, 492–495.
[58] M. W. Terban, S. J. L. Billinge, *Chem. Rev.* **2022**, *122*, 1208–1272.
[59] C. L. Farrow, P. Juhas, J. W. Liu, D. Bryndin, E. S. Božin, J. Bloch, T. Proffen, S. J. L. Billinge, *J. Phys.: Condens. Matter* **2007**, *19*, 335219.
[60] D. Umeyama, N. P. Funnell, M. J. Cliffe, J. A. Hill, A. L. Goodwin, Y. Hijikata, T. Itakura, T. Okubo, S. Horike, S. Kitagawa, *Chem. Commun.* **2015**, *51*, 12728–12731.
[61] H. Vogel, *J. Phys. Z* **1921**, *22*, 645–646.
[62] G. S. Fulcher, *J. Am. Ceram. Soc.* **1925**, *8*, 339–355.
[63] G. Tammann, W. Hesse, *Z. Anorg. Allg. Chem.* **1926**, *156*, 245–257.
[64] M. A. B. H. Susan, T. Kaneko, A. Noda, M. Watanabe, *J. Am. Chem. Soc.* **2005**, *127*, 4976–4983.
[65] C. Schreiner, S. Zugmann, R. Hartl, H. J. Gores, *J. Chem. Eng. Data* **2010**, *55*, 4372–4377.
[66] K. M. Diederichsen, H. G. Buss, B. D. McCloskey, *Macromolecules* **2017**, *50*, 3831–3840.
[67] W. Xu, C. A. Angell, *Science* **2003**, *302*, 422–425.
[68] L. Vilčiauskas, M. E. Tuckerman, G. Bester, S. J. Paddison, K.-D. Kreuer, *Nat. Chem.* **2012**, *4*, 461–466.
[69] J.-P. Melchior, K.-D. Kreuer, J. Maier, *Phys. Chem. Chem. Phys.* **2017**, *19*, 587–600.
[70] T. E. Faber, J. M. Ziman, *Philos. Mag.* **1965**, *11*, 153–173.
[71] E. Lorch, *J. Phys. C: Solid State Phys.* **1969**, *2*, 229–237.
[72] R. H. Blessing, *Acta Cryst* **1988**, *44*, 334–340.
[73] T. Norby, *Solid State Ion.* **1999**, *125*, 1–11.
[74] S. Kohara, M. Itou, K. Suzuya, Y. Inamura, Y. Sakurai, Y. Ohishi, M. Takata, *J. Phys. Condens. Matter.* **2007**, *19*, 506101.
[75] S. Bureekaew, S. Horike, M. Higuchi, M. Mizuno, T. Kawamura, D. Tanaka, N. Yanai, S. Kitagawa, *Nat. Mater.* **2009**, *8*, 831–836.
[76] J. A. Hurd, R. Vaidhyanathan, V. Thangadurai, C. I. Ratcliffe, I. L. Moudrakovski, G. K. H. Shimizu, *Nat. Chem.* **2009**, *1*, 705–710.
[77] D. Umeyama, S. Horike, M. Inukai, Y. Hijikata, S. Kitagawa, *Angew. Chem. Int. Ed.* **2011**, *50*, 11706–11709.
[78] D. Umeyama, S. Horike, M. Inukai, T. Itakura, S. Kitagawa, *J. Am. Chem. Soc.* **2012**, *134*, 12780–12785.
[79] S. S. Nagarkar, S. M. Unni, A. Sharma, S. Kurungot, S. K. Ghosh, *Angew. Chem. Int. Ed.* **2014**, *53*, 2638–2642.
[80] Q. Tang, Y. Liu, S. Liu, D. He, J. Miao, X. Wang, G. Yang, Z. Shi, Z. Zheng, *J. Am. Chem. Soc.* **2014**, *136*, 12444–12449.
[81] Y. H. Lei, N. Sheng, A. Hyono, M. Ueda, T. Ohtsuka, *Prog. Org. Coat.* **2014**, *77*, 339–346.
[82] S.-S. Yu, S.-X. Liu, H.-B. Duan, *Dalton Trans.* **2015**, *44*, 20822–20825.
[83] W. Chen, S. Horike, D. Umeyama, N. Ogiwara, T. Itakura, C. Tassel, Y. Goto, H. Kageyama, S. Kitagawa, *Angew. Chem. Int. Ed.* **2016**, *55*, 5195–5200.
[84] M. Inukai, S. Horike, T. Itakura, R. Shinozaki, N. Ogiwara, D. Umeyama, S. Nagarkar, Y. Nishiyama, M. Malon, A. Hayashi, T. Ohhara, R. Kiyanagi, S. Kitagawa, *J. Am. Chem. Soc.* **2016**, *138*, 8505–8511.
[85] Y.-S. Wei, X.-P. Hu, Z. Han, X.-Y. Dong, S.-Q. Zang, T. C. W. Mak, *J. Am. Chem. Soc.* **2017**, *139*, 3505–3512.
[86] Y. Ohara, A. Hinokimoto, W. Chen, T. Kitao, Y. Nishiyama, Y.-l. Hong, S. Kitagawa, S. Horike, *Chem. Commun.* **2018**, *54*, 6859–6862.
[87] S. Pili, P. Rought, D. I. Kolokolov, L. Lin, I. da Silva, Y. Cheng, C. Marsh, I. P. Silverwood, V. García Sakai, M. Li, J. J. Titman, L. Knight, L. L. Daemen, A. J. Ramirez-Cuesta, C. C. Tang, A. G. Stepanov, S. Yang, M. Schröder, *Chem. Mater.* **2018**, *30*, 7593–7602.
[88] K. I. Hadjiivanov, D. A. Panayotov, M. Y. Mihaylov, E. Z. Ivanova, K. K. Chakarova, S. M. Andonova, N. L. Drenchev, *Chem. Rev.* **2021**, *121*, 1286–1424.
[89] K. Zhang, G.-H. Wen, X.-J. Yang, D.-W. Lim, S.-S. Bao, M. Donoshita, L.-Q. Wu, H. Kitagawa, L.-M. Zheng, *ACS Materials Lett* **2021**, *3*, 744–751.
[90] J. N. Yankwa Djobo, R. Y. Nkwaju, *RSC Adv.* **2021**, *11*, 32258–32268.
[91] K. Takahashi, T. Ogawa, T. Itakura, K. Kami, S. Horike, *ACS Appl. Energy Mater.* **2024**, *7*, 11937–11945.

Manuscript received: February 25, 2025
Revised manuscript received: May 15, 2025
Accepted manuscript online: May 19, 2025
Version of record online: May 26, 2025